Carrier-envelope shearing and isolated attosecond pulse generation

A. Lotti,[1,2,*] D. Faccio,[1,3] A. Couairon,[2] M. B. Gaarde,[4] and P. Di Trapani[1]

[1]*Consorzio Nazionale Interuniversitario per le Scienze Fisiche della Materia and Department of Physics and Mathematics, Università dell'Insubria, I-22100 Como, Italy*

[2]*Centre de Physique Théorique, École Polytechnique, Centre National de la Recherche Scientifique, F-91128 Palaiseau, France*

[3]*School of Engineering and Physical Sciences, Scottish Universities Physics Alliance, Heriot-Watt University, Edinburgh, Scotland EH14 4AS, United Kingdom*

[4]*Department of Physics and Astronomy, Louisiana State University, Baton Rouge, Louisiana 70803-4001, U.S.A.*

(Received 21 February 2011; published 3 May 2011)

Conical Bessel-like pulses allow control of the propagation velocity of the main intensity peak. With few-cycle pulses, this leads to a controllable shearing effect with respect to the carrier-phase oscillation and a consequent variation of the instantaneous intensity during propagation. Numerical simulations highlight how this intensity modulation directly controls the atomic dipole phase in the process of high-order harmonic generation and isolates either the long or the short electron-trajectory contributions. We identify a propagation regime in which the harmonic field takes the form of an isolated pulse of 300 as duration.

DOI: 10.1103/PhysRevA.83.053804 PACS number(s): 42.65.Ky, 42.65.Re, 42.25.Bs, 42.65.Sf

I. INTRODUCTION

High-order harmonic generation (HHG) in gases has been thoroughly characterized in terms of the spectral range, brightness, spatial and temporal coherence, beam divergence, and pulse duration of the harmonic emission [1–4]. High-order harmonic generation is now used as a versatile and tunable source for the synthesis of the shortest events ever produced in a laser laboratory, lasting no more than tens to hundreds of attoseconds (as) [5] which are in turn used as probes for time-resolved studies of ultrafast dynamics of electronic wave packets in various physical systems [6,7].

High-order harmonic generation and, more generally, nonlinear light-matter interaction driven with few-cycle laser pulses, strongly depends on both (i) phase-matching [8,9], as in all frequency conversion processes, and (ii) the carrier-envelope phase (CEP) of the driver pulse (i.e., the relative shift between the maximum of the real electric field and that of the envelope). Below we will discuss these in turn.

(i) Phase-matching. The main contributions to the phase mismatch in HHG arise from geometric dispersion (related to the pulse-focusing properties), self-induced plasma dispersion, gas dispersion, and the atomic dipole phase. The atomic dipole phase is determined by the intensity gradient along the propagation direction and it is related to the specific trajectory the electron follows in the continuum, under the influence of the driving electric field. Usually only the first two trajectories, referred to as the long and short trajectories, are relevant in HHG. The phase-matching conditions can be controlled to some extent by balancing out the various effects. However, the contribution of the atomic dipole phase term is usually directly related to the focusing conditions when the beam is focused in a gas jet [10,11] and cannot be tuned beyond moving the relative position of the focus and the jet. Such a consideration may not hold for very short pulses (e.g., shorter than 3–4 optical cycles, where effects related to the z variation of the CEP may occur). In particular, the use of non-Gaussian pulses may allow the possibility of tuning such an effect by means of the control of the local intensity of field extrema during the propagation.

(ii) The carrier-envelope phase. At a given propagation distance z, the CEP of a few-cycle driver pulse usually undergoes shot-to-shot variations that severely affect HHG. Recently a number of techniques have been introduced in order to measure [12] and stabilize the CEP in time [13]. However, very few attempts have been made to control the CEP, not only from shot-to-shot, but also during the propagation of the light pulse. In principle, this control may be obtained by tuning the dispersion properties of the medium [14] or the properties of the pulse itself [15].

In this paper, we propose a spatial control mechanism for the phase-matching conditions in HHG by the use of intense few-cycle driving pulses in the form of conical (i.e., Bessel-like) wave packets (CWs), thereby allowing for predetermined relative propagation velocities of the envelope and carrier waves and tunable CEP along the propagation distance. Our numerical simulations of HHG by intense few-cycle CWs in a low-pressure argon gas exhibit a shearing effect that acts directly on the atomic-dipole-phase term, which in turn modifies the phase-matching conditions for the long and short electron-trajectory contributions to the HHG process. By controlling the amount of the CEP in shear, we also identify conditions for which the harmonic field appears directly in the form of an almost isolated pulse without any postprocess synthesis (e.g., additional filtering or compression stages).

II. CONICAL WAVE PACKETS

Conical wave packets are the axisymmetric counterparts of tilted pulses and may be viewed as a superposition of plane waves with frequency-dependent transverse components of wave vector $k_\perp$ distributed over cones with axes along the propagation direction z and angle $\theta(\omega)$ (see Refs. [16,17]). As schematically represented in Fig. 1, it is possible to independently tune phase (v_p) and envelope (v_e) velocities of the main-intensity peak of CWs by properly adjusting the

*antonio.lotti@uninsubria.it

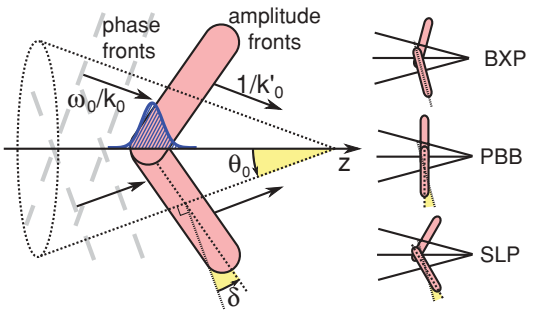

FIG. 1. (Color online) Schematic propagation of a CW: the gray dashed lines represent phase fronts and the red areas amplitude fronts. θ_0 and δ are the propagation and tilt angles, respectively. Note that the quantities v_p and v_e refer to the main-intensity peak of the pulse, represented in the figure by the blue Gaussian profile. On the right there is a schematic representation of the PBB, BXP, and SLP cases, as defined in the text.

propagation angle and angular dispersion. In particular, these velocities read [16]

$$v_p = \frac{\omega_0}{k_0 \cos\theta_0}, \tag{1}$$

$$v_e = \frac{\cos\delta}{k_0' \cos(\theta_0 + \delta)}, \tag{2}$$

with $\theta_0 = \theta(\omega_0)$ the mean cone angle, δ the tilt angle of the amplitude fronts, and $k_0^{(n)} = \partial^n k/\partial\omega^n|_{\omega=\omega_0}$, where ω_0 is the central frequency of the wave packet. It is important to emphasize that these velocities refer to the main-intensity peak of the pulse and, in particular, that v_e is not to be confused with the group velocity at which the amplitude fronts propagate.

In the ideal case, the difference between phase and envelope velocity determines a constant slipping of the field profile of the pump under the envelope so that the local maxima seem to be sheared by the motion of the envelope. This effect is expected to crucially influence highly nonlinear processes such as high-harmonic generation, since it introduces a modulation of the field extrema [18].

III. NUMERICAL MODEL

Our model is adapted from that of Refs. [19,20] and relies on a unidirectional propagation equation along the z direction for the frequency components $\tilde{E}(r,z,\omega)$ of the electric field $E(r,z,t)$ of the laser pulse and of the harmonic field generated by the pulse

$$\frac{\partial\tilde{E}}{\partial z} = i\left[\frac{\Delta_\perp}{2k(\omega)} + k(\omega) - \frac{\omega}{v_g}\right]\tilde{E} + \frac{\mu_0\omega}{2k(\omega)}(i\omega\tilde{P}_{\rm NL} - \tilde{J}), \tag{3}$$

where we are considering the field in the reference frame moving at the group velocity $v_g = (k_0')^{-1}$. $\tilde{P}_{\rm NL}(r,z,\omega)$ and $\tilde{J}(r,z,\omega)$ are the Fourier-transformed nonlinear polarization and current. The right-hand side of Eq. (3) models different effects depending on whether frequency components correspond to the laser pulse ($\omega < 10\omega_0$) or to the harmonic field ($\omega > 10\omega_0$). For the laser pulse, the nonlinear polarization includes the optical Kerr response $P_{\rm Kerr}(r,z,t) = \epsilon_0\chi^{(3)}E^3(r,z,t)$ described by the third-order susceptibility χ^3 (we used the value deduced from the measurements of [21]) and the plasma-induced current which comprises two parts: (i) Plasma-induced defocusing is accounted for by $J_{\rm Plasma}(r,z,t)$, where $\partial J_{\rm Plasma}/\partial t = (e^2/m_e)N_e E$, $N_e(r,z,t)$ denotes the density of electrons generated by optical field ionization and e and m_e denote the electron charge and mass. (ii) Nonlinear losses are accounted for by $J_{\rm NLL}(r,z,t)$ where $J_{\rm NLL} = [W(|E|)/|E|^2]N_{\rm Ar}U_i E$, $N_{\rm Ar}(r,z,t)$ denotes the density of nonionized argon atoms, U_i the ionization potential of argon, and $W(|E|)$ the field-dependent ionization rate. Ionization is described by an evolution equation for the density of argon atoms $\partial N_{\rm Ar}/\partial t = -W(|E|)N_{\rm Ar}$, from which the electron density is obtained by conservation $N_e(r,z,t) = N_0 - N_{\rm Ar}(r,z,t)$. For the harmonic field, the nonlinear polarization is obtained from the time-dependent dipole moment, calculated using the strong-field approximation [22] multiplied by the density of argon atoms. Its implementation strictly follows Ref. [19]. Dispersion of the pump field is calculated by means of the formula given in [23], while dispersion and absorption for the harmonic field come from the interpolation of the data given in [24].

IV. SIMULATIONS AND DISCUSSION

Our calculations start with 800-nm laser pulses with Gaussian 5-fs full width at half maximum (FWHM) temporal profile and peak electric field E_0 corresponding to an initial cycle-averaged intensity of 2.7×10^{14} W/cm^2, in the shape of CWs multiplied by a spatial apodizing Gaussian function in order to have finite total energy. We calculate the propagation of these pulses and HHG following the model of Eq. (3).

We considered three particular cases of CWs, which correspond to different values of the tilt angle for a given propagation angle: a pulsed Bessel beam (PBB), a Bessel-X pulse (BXP), and a superluminal pulse (SLP). More specifically, the plane-wave constituents of the PBB present equal transverse components of the k vector ($\delta = -\theta_0$) [16,25] and those of the BXP present equal propagation angle for each frequency ($\delta = 0$) [26]. The PBB exhibits subluminal velocity (i.e., its envelope velocity is smaller than its phase velocity $v_e < v_p$) while the BXP exhibits luminal velocity (i.e., $v_e \simeq v_p$). BXPs are typically generated experimentally by means of axicon lenses, while PBBs can be obtained by circular diffraction gratings or by coupling Gaussian pulses into hollow core fibers. We considered a third case, featured by $\delta = +\theta_0$ (SLP), in order to have superluminal velocity $v_e > v_p$. To date, SLP-like pulses have never been experimentally generated, but they do appear spontaneously during filamentation of ultrashort pulses in Kerr media [27]. For all cases, a cone angle $\theta_0 = 0.44^\circ$ was used. The three types of input beams are schematically represented in Fig. 1. Equation (2) shows that the PBB and the SLP are merely particular cases of subluminal and superluminal propagating CWs.

For the BXP case, a dominant factor in determining the temporal profile of the generated harmonic field is the initial CEP, which varies little during propagation since $v_e \simeq v_p$. Figures 2(a) and 2(b) show the evolution of the temporal-envelope profile for the axial ($r = 0$) harmonic field as a function of the propagation distance in a 1.3-cm long argon

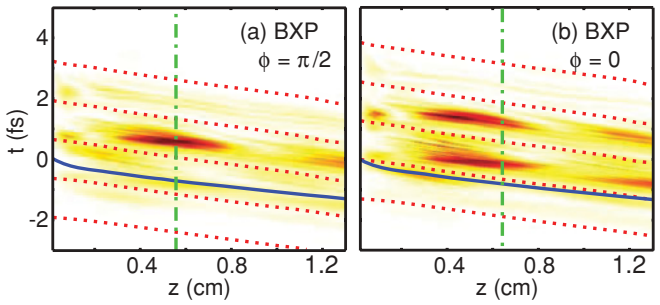

FIG. 2. (Color online) Axial time profile (linear scale) of the harmonic field versus propagation distance z for the BXP case for initial CEP (a) $\phi = \pi/2$ and (b) $\phi = 0$, synthesized with no further spectral filtering other than a high-pass filter $\omega > 10\omega_0$. The solid blue curves and the dashed red curves show the propagation of the center of mass (envelope peak) and the positions of squared field maxima of the driving infrared pulse, respectively. The vertical dashed-dotted lines mark the z positions of lowest ratio between the second most intense peak and the main peak for the $\phi = \pi/2$ case and the propagation distance chosen for Fig. 4(b) in the $\phi = 0$ case.

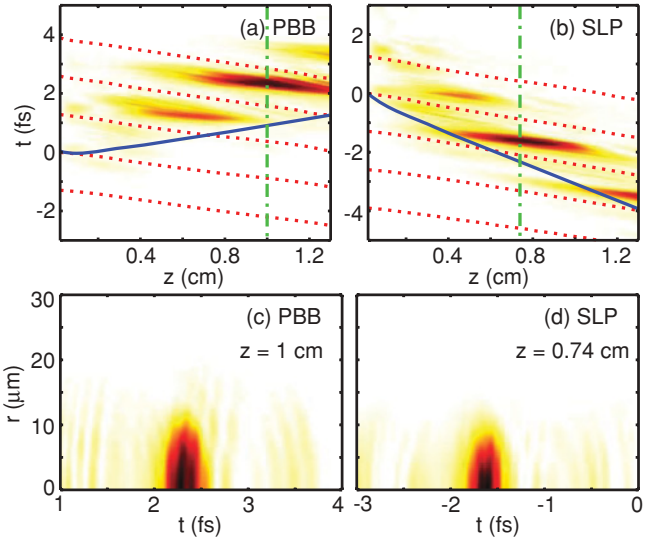

FIG. 3. (Color online) Axial time profile (linear scale) of the harmonic field versus propagation distance z for the (a) PBB and (b) SLP cases described in the text, synthesized with all the frequency contributions $\omega > 10\omega_0$. The solid blue curves and the dashed curves mark the propagation of the center of mass (envelope peak) of the driving infrared pulse and the positions of its squared field maxima, respectively. The vertical dashed-dotted lines mark the z positions chosen for Figs. 4. (c) and (d) show the near-field (r,t) envelope profile of the harmonic field (linear scale) for the PBB case at $z = 1$ cm and the SLP case at $z = 0.74$ cm, respectively.

gas at 100 mbars for two values of the initial CEP, $\phi = \pi/2$ and $\phi = 0$, respectively. The solid blue curve marks the peak of the envelope of the driving pulse; its slope is given by $1/v_e(z) - 1/v_g$. The dashed curves of slope $1/v_p(z) - 1/v_g$ mark the peaks of the driving field (maxima and minima) which move at phase velocity $v_p(z)$. The slopes of dashed and continuous lines are in agreement with the BXP property $v_e \simeq v_p$, except for effects related to the initial generation of plasma, which tends to defocus the trailing portion of the pulse, therefore shifting the position of the center of mass of the envelope, and a small correction related to Gaussian apodization [28]. The figures show a series of distinct extrema for the harmonic-field intensity along the temporal coordinate with durations of a few hundred attoseconds, which follow the peaks of the pump field with almost constant temporal delay along propagation. These harmonic bursts exhibit intensity oscillations along the propagation distance, which are related to phase-matching properties for the process.

We observe the generation of an almost isolated temporal peak in the harmonic field for the $\phi = \pi/2$ case, for which the ratio between the main peak and the second-most intense peak reaches the lowest value of 25% at $z = 0.56$ cm, with a corresponding FWHM duration of 340 as. We note that the selection of an isolated attosecond pulse would not occur in the absence of ionization gating, which in our case works mainly through the space- and time-dependent plasma-dispersion term. The plasma-refractive index causes a reshaping of the laser beam by advancing the peak of the laser pulse on axis, which effectively shortens the intense part of the pulse [29]. More importantly, the plasma contribution to the phase mismatch is time dependent, which means that the phase-matching conditions change from one half-cycle of the laser field to the next [30,31]. In the $\phi = \pi/2$ case, this leads to good phase-matching predominantly during one half-cycle of the driving field, whereas, in the $\phi = 0$ case, there are two half-cycles in which the harmonic radiation is phase-matched which leads to two attosecond bursts. These two bursts exhibit different time-frequency characteristics both in terms of their cutoff energy and in terms of the dominant quantum path contributions, consistent with a rapidly changing phase mismatch [31].

The results in Fig. 2 show that the generation of an isolated attosecond pulse by the BXP depends sensitively on the initial value of the laser CEP, just as in few-cycle Gaussian pulses. We expect this to remain true for all pulses in which $v_e \simeq v_p$. However, in the following we will show that the situation will differ substantially in the case when $v_e \neq v_p$: then, the CEP becomes a function of the propagation distance z so that at a certain point during propagation, the optimal CEP for isolated pulse generation will be encountered.

Figures 3(a) and 3(b) show the (z,t) evolution of the envelope profile for the axial $(r = 0)$ harmonic field, analogous to Fig. 2 for the PBB and SLP cases, respectively. Note that although the initial stage is affected by effects related to initial strong-plasma generation or to the Gaussian apodization, the slopes of the dashed and continuous lines (referring to the driving infrared field) are in agreement with the predictions of Eqs. (1) and (2) for the propagation of linear, nonapodized CWs, thereby justifying the comparison with velocities of ideal, infinitely extended CWs.

These figures clearly show effects related to the envelope velocity (i.e., during propagation, the position of the envelope maximum shifts and is sheared with respect to the carrier-wave propagation). This, in turn, gradually modifies the intensities of the field maxima and, accordingly, the related HHG process. We observe that the harmonic field is still generated along the isophase lines of the pump field in the (z,t) space, but the shift of the pump envelope induces a shearing in the harmonic peak, which is negative (i.e., delayed) for the PBB case and positive

(i.e., advanced) for the SLP case. The harmonic field still exhibits intensity oscillations along z, but these are displaced following the direction of the pump envelope velocity. In the BXP case, we do not observe this phenomenon because of equal phase and envelope velocities.

This shearing effect, in turn, continuously modifies the CEP of the pump wave packet and at a certain z position along propagation it reduces to the optimal value for the generation of an almost isolated temporal peak in the harmonic field, similarly to Fig. 2(a). In particular, from the simulations we observe a 350–400-as pulse for the PBB case between $z = 0.9$ cm and $z = 1.2$ cm. The ratio of the second-highest peak to the intensity of the main peak is below 35% and the minimum ratio is 16% at $z = 1$ cm, with a corresponding duration (FWHM) of 350 as. Note that we did not perform any other spectral filtering on the harmonic field except for a high-pass filter at $10\omega_0$, mimicking the action of an aluminum filter frequently used in experiments to separate the laser light from the harmonic light. We obtained a 300–320-as pulse for the SLP case between $z = 0.65$ cm and $z = 0.9$ cm, with contrast below 35%, which reaches a minimum of 13.5% at $z = 0.74$ cm, with a corresponding duration of 300 as.

The radial profiles of the envelope of the harmonic field in the PBB and SLP cases are shown in Figs. 3(c) and 3(d), respectively, highlighting the smooth spatiotemporal profiles of the harmonic pulses that are spatially confined on axis within a 20-μm radius. The total attosecond pulse energies are 23 pJ and 8 pJ for the PBB and SLP cases, respectively.

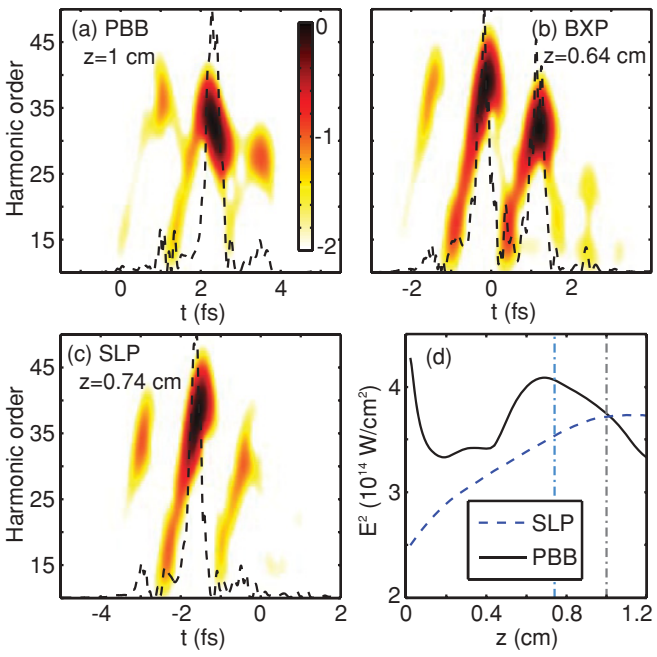

FIG. 4. (Color online) Temporal gated spectra of the harmonic field (logarithmic scale over two decades) generated by CWs at given propagation distance: (a) PBB at $z = 1$ cm, (b) BXP ($\phi = 0$) at $z = 0.64$ cm, and (c) SLP at $z = 0.74$ cm. The dashed lines represent the temporal-envelope profile of the harmonic field. (d) Instantaneous values of E^2 as a function of propagation distance for the pump peak giving the main contribution to the almost isolated harmonic pulses, in the PBB (black solid) and SLP (blue dashed) cases. The vertical dashed-dotted lines mark the z positions of (a) and (c).

The shearing effect on HHG was further investigated by considering the time-frequency dependence of the harmonic field at the point of best contrast for the cases PBB and SLP, and comparing it to the BXP case with $\phi = 0$. We show these spectra over two decades in Fig. 4. The dashed lines represent the temporal-envelope profiles of the harmonic field. The figures show that the shearing effect not only affects the temporal profile of the harmonic field, but also acts as a gating mechanism in the spectral domain. In particular, in the BXP case [Fig. 4(b)], the portions of the spectrum corresponding to the temporal peaks fall in the region around the cutoff. These regions come from both short- and long-path contributions [19]. In the PBB and SLP cases [Fig. 4(a) and 4(c), respectively], the main contributions come from regions near the cutoff, but may now be identified as corresponding to long (PBB case) and short (SLP case) paths. We also directly verified that the angular spread (data not shown) in the PBB case (0.81 mrad) is slightly larger with respect to the SLP case (0.73 mrad), in keeping with the standard observation that contributions from long trajectories exhibit a larger divergence than those of short trajectories [19].

V. QUANTUM TRAJECTORY CONTRIBUTIONS

The selection of contributions of different quantum trajectories may be explained qualitatively by considering the evolution of the instantaneous intensity (squared electric field) maxima of the driving field along propagation in the different cases. In particular, the intensity of the pump peak corresponding to the harmonic burst associated with the isolated pulse is increasing versus propagation distance around $z = 0.74$ cm in the SLP case and decreasing around $z = 1$ cm in the PBB case, as illustrated by Fig. 4(d). This determines different signs for the dipole-phase-contribution term for the

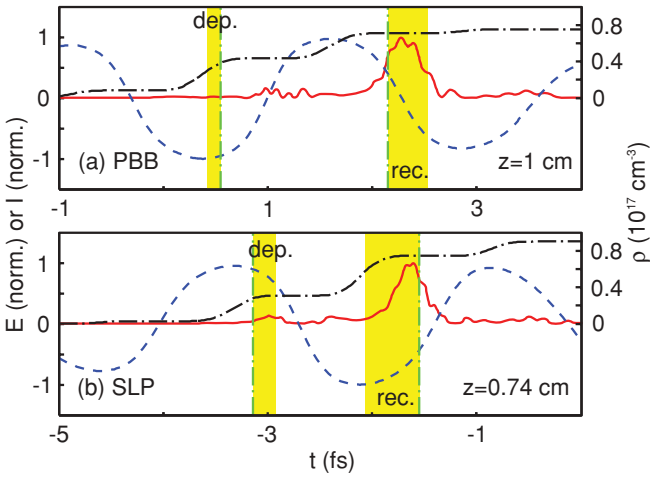

FIG. 5. (Color online) Blue dashed line: electric field of the pump (normalized; left axis); red continuous line: envelope of the harmonic field (normalized; left axis); black dashed-dotted line: plasma density (right axis), at $r = 0$ versus time for a) PBB at $z = 1$ cm and b) SLP at $z = 0.74$ cm. The yellow areas represent the departure (*dep.*) and recollision (*rec.*) times for the electrons in the two cases from the classical approach. The vertical green dashed-dotted lines refer to the trajectories whose return energy correspond to the cutoff.

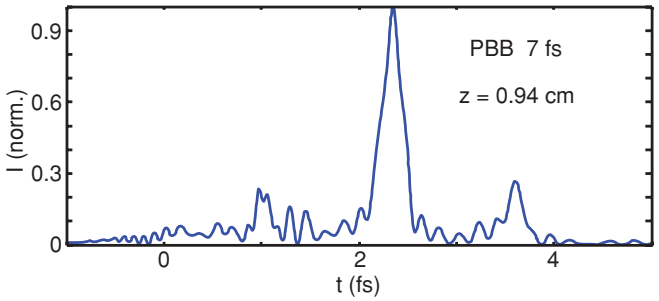

FIG. 6. (Color online) Temporal profile on axis of the envelope of the harmonic field in the position of best contrast ($z = 0.94$ cm) for the input case of a PBB with FWHM duration 7 fs.

different cases [32]. By adopting the sign convention of [19], we may isolate each contribution to the phase-matching for the harmonic field generation. The geometric term is always positive for both PBB and SLP, since the effective pump wave vector on axis is shortened in CWs [33–35]. The plasma contribution is positive as well and similar for both cases, as shown in Fig. 5 by the temporal profiles of the on-axis plasma density in the corresponding region of electron emission. The dipole term depends on the gradient along propagation of the instantaneous intensity and is negative for the PBB and positive for the SLP. In both cases, the absolute value of the dipole contribution will be small and close to zero for short trajectories and large for long trajectories [36,37]. Therefore, the large positive δk contribution in the PBB case may be compensated, or partially compensated, for by the large negative dipole contribution from the long trajectories. However, in the SLP case, all the contributions are positive and the minimum δk is obtained for the smallest possible dipole term (i.e., the short-trajectory term).

We stress that, in the CW case, the z evolution of the intensity is not determined by the apodization (i.e., Gaussian focusing) of the beam, but by the difference between phase and envelope velocities. This effect is thus expected to be relevant only for very short pulses, such as the 5-fs pulses of this work. Our calculations showed that the shearing effect is significantly reduced with 12-fs pulses, however, we verified that isolated attosecond pulses are still generated using relatively accessible 7-fs pulses. We considered a PBB under exactly the same conditions as described above (gas pressure, CW cone angle, and tilt) and we obtained a minimum FWHM duration for the harmonic field of 245 as at $z = 0.94$ cm [Fig. 6], albeit with a slightly lower contrast of nearly 28%.

VI. CONCLUSION

In conclusion, we have studied the role of envelope velocity and CEP shearing in HHG with conical-wave driving pulses. We found that the difference between envelope and phase velocities due to the space-time structure of such pulses has important consequences for HHG, most notably the selection of different quantum path contributions and the generation of isolated attosecond pulses. These effects are most evident for very short pulses (less than three optical cycles) due to the fact that they rely on the instantaneous variation of the local intensity of the pump field (i.e., on the variation of the CEP in propagation). We emphasize that given the phase-matching nature of the process, for a given gas and gas pressure, there is an optimal value of the Bessel cone angle that achieves isolated pulse generation, since this relies on an ionization-gating mechanism. This angle was found by scanning over different angle values, although in an experiment it would be easier to scan over the gas pressure. We found an optimal cone angle of 0.44°. While the technology to generate a SLP has yet to be developed, a 5–7-fs PBB may be readily obtained by generating the harmonics in an appropriate hollow-core fiber [38]. Indeed, the modes of these fibers are precisely PBBs and the fundamental-mode cone angle is related to the fiber diameter d by $d = 2.4048 \times (2c)/\omega_0 \sin\theta_0$. The 0.44° cone angle used in this work may be obtained with an 80-μm diameter fiber and isolated attosecond pulse generation with acceptable contrast may be obtained under realistic and simple experimental conditions. In this case, calculations would need to be performed to account for the modifications induced by the fiber geometry with respect to the free-space geometry, such as a slightly modified v_e, linear losses, and dispersion. However, over the considered distances (1–2 cm), we expect these to be minor perturbations and, therefore, to still observe the dynamics highlighted in this work.

ACKNOWLEDGMENTS

PDT and DF acknowledge financial support from the Consorzio Nazionale Interuniversitario per le Scienze Fisiche della Materia (CNISM), INNESCO project. This work was supported in part by the National Science Foundation under Grant No. PHY-0449235.

[1] P. Salières, A. L'Huillier, Ph. Antoine, and M. Lewenstein, Adv. At. Mol. Opt. Phys. **41**, 83 (1999).
[2] T. Brabec and F. Krausz, Rev. Mod. Phys. **72**, 545 (2000).
[3] H. C. Kapteyn, O. Cohen, I. Chrisotv, and M. M. Murnane, Science **317**, 775 (2007).
[4] T. Popmintchev, M-C. Chen, P. Arpin, M. M. Murnane, and H. C. Kapteyn, Nature Photon. **4**, 822 (2010).
[5] F. Krausz and M. Ivanov, Rev. Mod. Phys. **81**, 163 (2009).
[6] J. Itatani, J. Levesque, D. Zeidler, H. Niikura, H. Pépin, J. C. Kieffer, P. B. Corkum, and D. M. Villeneuve, Nature (London) **432**, 867 (2004).
[7] M. Hentschel, R. Kienberger, Ch. Spielmann, G. A. Reider, N. Milosevic, T. Brabec, P. Corkum, U. Heinzmann, M. Drescher, and F. Krausz, Nature (London) **414**, 509 (2001).
[8] A. Paul, E. A. Gibson, X. Zhang, A. Lytle, T. Popmintchev, X. Zhou, M. M. Murnane, I. P. Christov, and H. C. Kapteyn, IEEE J. Quantum Electron. **42**, 14 (2006).
[9] A. Bahabad, M. M. Murnane, and H. C. Kapteyn, Nature Photon. **4**, 570 (2010).
[10] Ph. Antoine, A. L'Huillier, and M. Lewenstein, Phys. Rev. Lett. **77**, 1234 (1996).

[11] M. B. Gaarde and K. J. Schafer, Phys. Rev. Lett. **89**, 213901 (2002).
[12] G. G. Paulus, F. Lindner, H. Walther, A. Baltuska, and F. Krausz, J. Mod. Opt. **52**, 221 (2005).
[13] T. Fuji, J. Rauschenberger, Ch. Gohle, A. Apolonski, T. Udem, V. S. Yakovlev, G. Tempea, T. W. Hänsch, and F. Krausz, New J. Phys. **7**, 116 (2005).
[14] M. A. Porras and P. Dombi, Opt. Express **17**, 19424 (2009).
[15] D. Faccio, A. Lotti, M. Kolesik, J. V. Moloney, S. Tzortzakis, A. Couairon, and P. Di Trapani, Opt. Express **16**, 11103 (2008).
[16] M. A. Porras, G. Valiulis, and P. Di Trapani, Phys. Rev. E **68**, 016613 (2003).
[17] *Localized Waves*, edited by H. E. Hernández-Figueroa, M. Zamboni-Rached, and E. Recami, (Wiley Interscience, New York, 2008).
[18] D. Faccio, C. Serrat, J. M. Cela, A. Farrés, P. Di Trapani, and J. Biegert, Phys. Rev. A **81**, 011803 (2010).
[19] M. B. Gaarde, J. L. Tate, and K. J. Schafer, J. Phys. B **41**, 132001 (2008).
[20] M. B. Gaarde and A. Couairon, Phys. Rev. Lett. **103**, 043901 (2009).
[21] D. P. Shelton, Phys. Rev. A **42**, 2578 (1990).
[22] M. Lewenstein, Ph. Balcou, M. Y. Ivanov, A. L'Huillier, and P. B. Corkum, Phys. Rev. A **49**, 2117 (1994).
[23] A. Bideau-Mehu, R. Guern, Y. Abjean, and A. Johannin-Gilles, J. Quant. Spectrosc. Radiat. Transfer **25**, 395 (1981).
[24] [http://www.cxro.lbl.gov/].
[25] F. Gori, G. Guattari, and C. Padovani, Opt. Commun. **64**, 491 (1987).
[26] P. Saari and K. Reivelt, Phys. Rev. Lett. **79**, 4135 (1997).
[27] D. Faccio, M. A. Porras, A. Dubietis, F. Bragheri, A. Couairon, and P. Di Trapani, Phys. Rev. Lett. **96**, 193901 (2006).
[28] Z. L. Horváth, J. Vinkó, Zs. Bor, and D. von der Linde, Appl. Phys. B **63**, 481 (1996).
[29] M. B. Gaarde and K. J. Schafer, Opt. Lett. **31**, 3188 (2006).
[30] C. A. Haworth, L. E. Chipperfield, J. S. Robinson, P. L. Knight, J. P. Marangos, and J. W. G. Tisch, Nature Phys. **3**, 52 (2007).
[31] M. J. Abel, T. Pfeifer, P. M. Nagel, W. Boutu, M. J. Bell, C. P. Steiner, D. M. Neumark, and S. R. Leone, Chem. Phys. **366**, 9 (2009).
[32] Ph. Balcou and A. L'Huillier, Phys. Rev. A **47**, 1447 (1993).
[33] C. Altucci *et al.*, Phys. Rev. A **68**, 033806 (2003).
[34] T. Auguste, O. Gobert, and B. Carré, Phys. Rev. A **78**, 033411 (2008).
[35] A. Averchi, D. Faccio, R. Berlasso, M. Kolesik, J. V. Moloney, A. Couairon, and P. Di Trapani, Phys. Rev. A **77**, 021802 (2008).
[36] M. Lewenstein, P. Salières, and A. L'Huillier, Phys. Rev. A **52**, 4747 (1995).
[37] Ph. Balcou, P. Salières, A. L'Huillier, and M. Lewenstein, Phys. Rev. A **55**, 3204 (1997).
[38] M. Nisoli *et al.*, Phys. Rev. Lett. **88**, 033902 (2002).